Journal of Advanced Ceramics
先进陶瓷
ISSN 2226-4108
CN 10-1154/TQ
清华大学出版社 Tsinghua University Press
SciOpen

J Adv Ceram 2026, **15**: 9221401

https://doi.org/10.26599/JAC.2026.9221401

Research Article

Ultrahigh strain in BF–BT ceramics via synergistic optimization of defect dipoles and electric field gradient

Huangtao Wu, Zhibo Chen, Jinbo Zhao, Zhen Zhang, Hongyu Yang*,

Linzhuang Xing*, Zhimin Li*

School of Advanced Materials and Nanotechnology, Xidian University, Xi'an 710071, China.

* Corresponding author.

E-mail: H. Yang, yanghongyu@xidian.edu.cn;

L. Xing, lzxing@xidian.edu.cn;

Z. Li, lizhmin@163.com

Received: August 19, 2026; Revised: September 30, 2026; Accepted: October 28, 2026

©The Author(s) 2026

Just Accepted

清华大学出版社 Tsinghua University Press | SciOpen

Abstract: The development of high-performance lead-free piezoelectric ceramics is critical for advancing precision actuation equipment while mitigating the environmental toxicity associated with

lead-based materials. Herein, a synergistic strategy combining defect dipoles with electric field gradient was proposed to improve the strain characteristics of $BiFeO_3$–$BaTiO_3$ (BF–BT) ceramics. Through introducing the component $KTaO_3$ (KT), it is found that defect dipoles [$(Fe'_{Ti}$–$V_O^{\bullet\bullet})^{\bullet}$ and $(Mn''_{Ti}$ $-V_O^{\bullet\bullet})^{\times}$] and relaxor characteristics are mediated, and that a unique domain structure is also created in BF–BT–0.015KT ceramic, in which island domains are surrounded by stripe domains, showing fast response to external field. Moreover, reducing the sample thickness enables a significant increase in the electric field gradient at electrode edges, thereby enhancing the macroscopic strain induced by bending deformation. Finite element analysis results indicate that the electric field gradient at the electrode edge in thin samples is greater than that in thick samples by approximately one order of magnitude. Accordingly, an ultrahigh strain of 1.13%, a high Curie temperature of 374 °C, excellent cyclic stability (4×10^5 cycles, degrades by 7.9%), and good thermostability (25–150 °C, varies by 8.3%) are simultaneously achieved in the BF–BT–0.015KT ceramic with a thickness of 0.15 mm and an electrode radius of 4 mm. The findings provide a novel perspective for understanding the bending deformation and identify a promising material for developing high-performance lead-free piezoelectric bending actuators.

Keywords: Piezoelectric ceramic; Strain; Defect dipole; Electric field gradient; Bending deformation

1 Introduction

Piezoelectric ceramic actuators are indispensable components in precision optical systems and emerging micro-electromechanical systems (EMES) [1,2], owing to their advantages of fast response, high positioning accuracy, and compact size, etc. In particular, recently reported piezoelectric bending actuators show great potential in the fields of flexible electronics and cantilever actuators [3,4]. Currently, commercial piezoelectric ceramic actuators mainly rely on lead zirconate titanate (PZT) ceramics, such as PZT–4 and PZT–5A [5], which benefit from their excellent electromechanical properties, good stability and low cost. However, lead-based materials may pose serious risks to the

Just Accepted

natural environment and human health during industrial production and daily use. Moreover, the EU's Restriction of Hazardous Substances (RoHS) directive explicitly restricts the use of elements such as lead and cadmium [6,7]. On the other hand, the operating temperature of PZT-based piezoelectric actuators is typically limited to below 150 ℃, which fails to meet the requirements of high-temperature applications such as energy exploration, deep-space exploration, and special-purpose equipment [8,9]. Therefore, it is imperative to develop high-temperature resistant lead-free piezoelectric actuators. Bismuth ferrite-barium titanate (BF–BT) piezoelectric ceramics are promising candidates for high-temperature lead-free piezoelectric actuators due to their high Curie temperature, strong piezoelectric response, and environmental friendliness [10–12]. Nevertheless, limited strain, large hysteresis, and high driving electric field limit the practical applications of BF–BT-based ceramics [11,13]. To date, researchers have employed several strategies including defect engineering, domain engineering, and texture engineering to address the above issues of BF–BT-based ceramics [14–16]. However, the strain of modified BF–BT ceramics remains below 0.5%, and this is often accompanied by a significant decrease in Curie temperature. Hence, achieving ultrahigh strain while retaining a high Curie temperature remains an urgent challenge for BF–BT-based ceramics.

Recently, several studies demonstrated that the size effect (such as grain size, sample thickness, etc.) can significantly enhance the strain performance of piezoelectric ceramics [17–20]. For example, Hou *et al*. [18] and Adhikary *et al*. [20] revealed that the observed ultrahigh strain originated not from the effect of a single defect dipole but from the synergistic interplay of multiple mechanisms. In thick samples, the electric field distribution between electrodes is essentially uniform. However, reducing the sample thickness to sub-millimeter scales leads to a notable enhancement of the local electric field at the electrode edges [21]. Moreover, differences in dielectric properties between grain boundaries and grains can also cause the redistribution of the electric field [22]. Consequently, this geometric change can induce a pronounced electric field gradient at grain boundaries and electrode edges. Domain dynamics theory indicates that a uniform electric field generates a unidirectional driving force

Just Accepted

on the domain walls [23]. In contrast, an electric field gradient can provide an additional driving force that promotes domain switching and significantly enhances domain wall migration, thereby achieving larger macroscopic strain [24,25]. In addition, recent discoveries demonstrated that the gradient distribution of intrinsic material properties (such as defect dipole concentration, piezoelectric coefficient, etc.) along the thickness direction can provide a driving force for obtaining ultrahigh strain exceeding 1% in systems such as (Na,K)NbO_3 and (Na,Bi)TiO_3 [26,27]. On the basis of the above observations, researchers proposed the concept of electric field-induced bending. The formula derived by Tan *et al*. [27] further indicated that bending strain is not only related to intrinsic material properties (d_{31} gradient), but also closely related to extrinsic factors such as the electric field (E), disk length (L, i.e. electrode effective diameter), and sample thickness (t). However, many studies attributed the ultrahigh strain resulting from bending deformation solely to gradient changes in intrinsic material properties, overlooking its synergistic dependence on both intrinsic material properties and extrinsic factors. Moreover, the dynamic visualization of the bending process was rarely reported, and techniques such as laser scanning and high-speed imaging can also difficult to clearly capture the bending deformation process.

In this work, we proposed a novel strategy to greatly enhance the strain performance of BF–BT-based piezoelectric ceramics through the synergistic optimization of defect dipoles (intrinsic factors) and electric field gradient (extrinsic factors). The electric field gradient is defined as the gradient of the in-plane electric field component (E_x) along the thickness direction. 0.7$BiFeO_3$–(0.3−x)$BaTiO_3$–$x$$KTaO_3$ (abbreviated as BF–BT–xKT, x = 0.000, 0.010, 0.015, and 0.020) piezoelectric ceramics were synthesized via the conventional solid-state reaction method. The introduction of KT promotes an increase in the concentration of defect dipoles [$(Fe'_{Ti}–V_O^{\bullet\bullet})^{\bullet}$ and $(Mn''_{Ti}–V_O^{\bullet\bullet})^{\times}$] in the ceramics, and endows the ceramics with enhanced relaxor characteristics, refined domain structure, and higher grain boundary density. These intrinsic microstructural factors are expected to significantly amplify the effect of the electric field gradient in boosting the strain response and facilitating domain switching.

Just Accepted

Simultaneously, reducing the sample thickness substantially increases the electric field gradient, which is beneficial for further enhancing the magnitude of macroscopic strain. More importantly, a finite element model was developed to confirm the existence of this electric field gradient and visually present the dynamic bending process. The optimized BF–BT–0.015KT ceramic achieves an ultrahigh strain of 1.13% and a high Curie temperature of 374 ℃ at a thickness of 0.15 mm and an electrode radius of 4 mm.

2 Experimental section

The BF–BT–*x*KT ceramics were prepared by solid-state reaction, with sample thicknesses (*t*) of 0.15, 0.20, and 0.50 mm and electrode radii (*r*) of 2, 3, and 4 mm as specified in the figure captions. Detailed experimental procedures are provided in the Electronic Supplementary Material (ESM).

3 Results and discussion

Figure 1(a) shows the XRD patterns and magnified diffraction peaks of the BF–BT–*x*KT ceramics. All samples exhibit a typical perovskite structure, and no obvious secondary phase is observed, indicating that $KTaO_3$ has uniformly diffused into the crystal lattice of the BF–BT ceramics. To preliminarily determine the phase structure of the BF–BT-based ceramics, the (110) and (111) diffraction peaks near 32° and 39° are amplified, as shown in the right panel of Fig. 1(a). The phase structure of BF–BT-based ceramics is usually composed of pseudocubic (PC) and rhombohedral (R) phases [28]. Accordingly, $BaTiO_3$ with a *Pm*3*m* structure (PDF#01-075-0461) and $BiFeO_3$ with an *R*3*c* structure (PDF#01-086-1518) were selected as references for the BF–BT–*x*KT ceramics of different KT contents. At $x = 0.000$, no obvious splitting of the diffraction peaks is observed, indicating that the PC phase dominates at this composition. However, the diffraction peaks exhibit distinct splitting with *x* increasing from 0.010 to 0.020, implying a phase transition from the PC phase to the R phase [29]. Meanwhile, the (111) diffraction peak gradually shifts toward lower angles, suggesting the presence of a slight lattice expansion. This phenomenon is attributed to the substitution of Ba^{2+} and Ti^{4+} at the A-site and B-site by K^+ and Ta^{5+}, respectively, which possess larger ionic radii than the original ions

Just Accepted

[30,31]. For x = 0.020, the (111) peak shifts slightly back toward higher angles, which may be related to the formation of complex defect dipoles at higher defect concentrations [32].

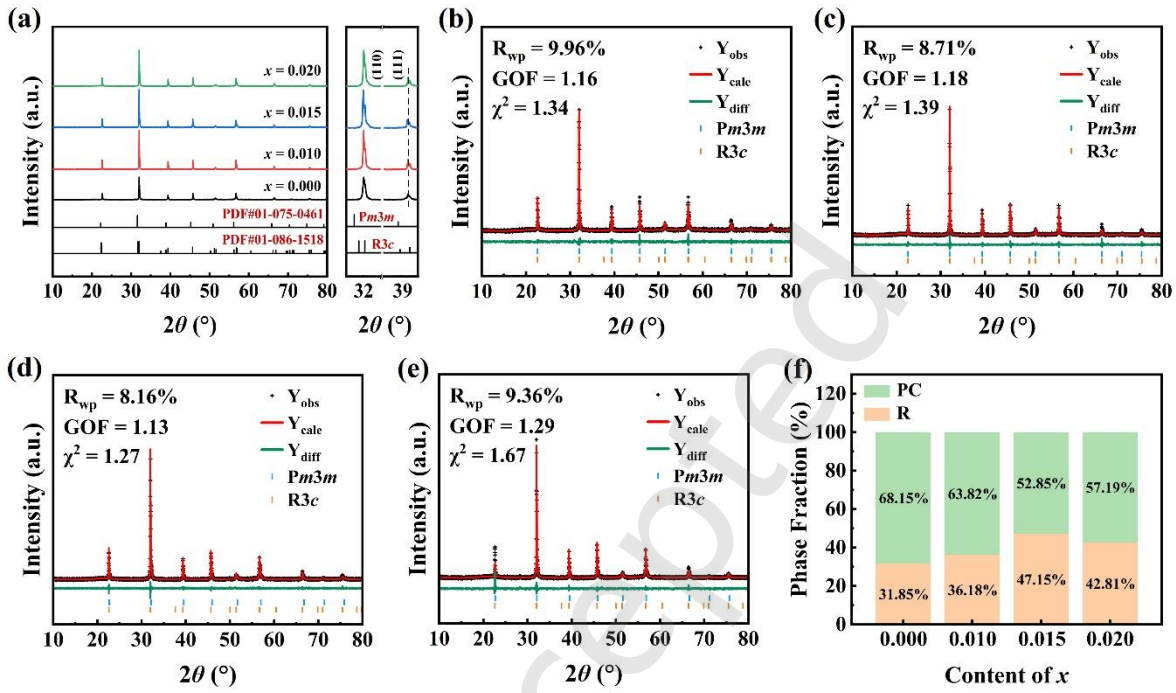

Fig. 1 (a) XRD patterns and magnified diffraction peaks around 32° and 39° of BF–BT–xKT ceramics. Rietveld refinement patterns of BF–BT–xKT ceramics for (b) x = 0.000, (c) x = 0.010, (d) x = 0.015, and (e) x = 0.020. (f) The variation of phase fraction in BF–BT–xKT ceramics with respect to x.

In order to deeply analyze the phase composition and cell parameters of the BF–BT–xKT ceramics, Rietveld refinement was performed and the results are summarized in Fig. 1(f) and Table S1 in the ESM. The corresponding Rietveld refinement patterns for different compositions are shown in Figs. 1(b)–1(e). As x increases, the fraction of the PC phase decreases from 68.15% to 57.19%, confirming the transformation from PC phase to R phase. Therefore, the lattice distortion in BF–BT–xKT ceramics primarily originates from the R phase [33]. In addition, it can be seen from Table S1 in the ESM that when x increases to 0.015, the unit cell volume of the R phase reaches the maximum value. As x continues to increase, the unit cell volume of R phase decreases slightly, which is consistent with the XRD results. It is noteworthy that at x = 0.015, the phase composition lies within the morphotropic phase boundary (MPB) region. This is beneficial for reducing polarization anisotropy and energy

Just Accepted

barrier for domain switching, thereby enhancing the strain performance of BF–BT-based ceramics and achieving a high Curie temperature [34,35].

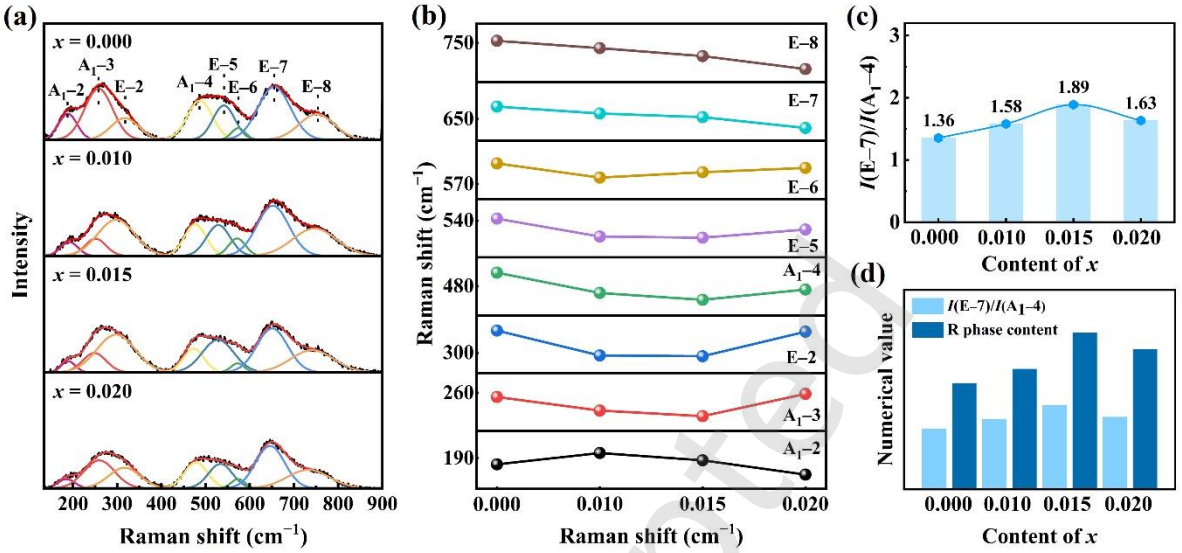

Fig. 2 BF–BT–*x*KT ceramics: (a) Raman spectra; (b) the peak positions of different Raman modes; (c) the value of I(E–7)/I(A$_1$–4); (d) the relationship between I(E–7)/I(A$_1$–4) value and R phase content.

The effect of $KTaO_3$ content on the local structure of the BF–BT ceramics was further investigated using Raman spectroscopy, as shown in Fig. 2(a). In general, $BiFeO_3$ exhibits 13 Raman active modes while $BaTiO_3$ shows 8 modes. Owing to the overlap of modes in BF–BT-based ceramics, only 8 Raman modes can be resolved here [36]. The Raman spectrum of BF–BT-based ceramics can be divided into three regions corresponding to different vibrational modes. The low wavenumber region ($\leq$ 150 cm^{-1}) reflects the vibration mode of A-site ions. The wavenumber range of 150–400 cm^{-1} represents the vibration mode of B-site ions (including Fe/Ti/Ta), mainly corresponding to the bending and stretching vibration of B–O bond. Modes in the range higher than 400 cm^{-1} indicate the vibration of the BO_6 octahedron, where modes of A$_1$–4 and E–7 are closely related to the distortion degree of the BO_6 octahedron [11,36]. As shown in Fig. 2(b), the A$_1$–3 and E–2 Raman modes display a significant shift toward the lower wavenumber range as x increases, indicating the gradual weakening in B–O bond [37]. When x = 0.015, the weakening of the B–O bond is most pronounced. This weakening is caused by defects introduced into the BF–BT ceramic lattice by the addition of KT. These charged defects are

Just Accepted

prone to combine and form defect dipoles, such as $(Fe'_{Ti}–V_O^{\bullet\bullet})^{\bullet}$ and $(Mn''_{Ti}–V_O^{\bullet\bullet})^{\times}$, which perturb the oxygen coordination environment around the defect centers and reduce the effective force constant of the B–O bond, thereby weakening the B–O bond strength [38–40].

To support this conclusion, low-temperature EPR tests were conducted on samples with x = 0.000 and 0.015, as shown in Figs. S1(a) and S1(b) in the ESM. Both samples exhibit similar resonance signals with g values of approximately 4.23 and 2.16. The signal at $g \approx 4.23$ is attributed to the Fe^{3+} and Mn^{2+} ions located at low symmetry lattice sites [41,42]. Further explanation can be given that in PZT ceramics, Zr and Ti elements occupy the B-site at the same valence, while in BF–BT ceramics, the B-site is co-occupied by Fe and Ti elements with different valences. This valence state difference allows Fe^{3+} ions occupying the B-site to be regarded as the acceptor center in the local structure, represented by Fe'_{Ti} defects. These Fe'_{Ti} defects will combine with adjacent oxygen vacancies to form $(Fe'_{Ti}–V_O^{\bullet\bullet})^{\bullet}$ defect dipoles, which is beneficial for minimizing system energy [43]. Oxygen vacancies can be provided by the bismuth volatilization and the partial reduction of Fe^{3+} ions. As reported for Fe^{3+}-doped PZT ceramics, the $(Fe'_{Ti}–V_O^{\bullet\bullet})^{\bullet}$ defect dipoles possess a large axial zero-field splitting parameter ($D \approx 35.28$ GHz) that far exceeds the microwave photon energy ($h\nu \approx 9.47$ GHz) [41,43]. This condition ($D \gg h\nu$) leads to the appearance of a resonance signal for $(Fe'_{Ti}–V_O^{\bullet\bullet})^{\bullet}$ in the low-field region [41]. Bykov *et al*. [44] also confirmed that the $g \approx 4.3$ signal in Fe^{3+}-doped PZT ceramics can be assigned to the $Fe^{3+}–V_O$ complex. On the other hand, $(Mn''_{Ti}–V_O^{\bullet\bullet})^{\times}$ defect dipoles also contribute to resonance signals in the low-field region [41]. Mn^{2+} ions (derived from Mn^{4+} ions transformed at high temperatures) located at low symmetry sites (rhombic) are expected to produce broadened lines rather than the six-line hyperfine structure [45]. Consequently, the resonance signal of $g \approx 4.23$ is manifested here as a broad composite peak, contributed by the resonance signals of $(Fe'_{Ti}–V_O^{\bullet\bullet})^{\bullet}$ and $(Mn''_{Ti}–V_O^{\bullet\bullet})^{\times}$ defect dipoles. The peak-to-peak linewidth (ΔB_{pp}) of this composite peak is 26 mT, corresponding to the g value range of 3.9–4.5. Moreover, the resonance signal observed at $g \approx 2.16$ is attributed to Fe^{3+} ions and their clusters in the less distorted octahedral cation positions [46]. Further comparison of the

Just Accepted

EPR signal intensities for samples with x = 0.000 and 0.015 reveals that this resonance signal is significantly enhanced with the increment of KT content. Specifically, the introduction of KT substantially raises the defect concentration (especially oxygen vacancies) within the lattice, effectively promoting the formation of defect dipoles. Notably, no anomalous broadening of the resonance peak is observed with increasing KT content. This finding indirectly confirms that the sample exhibits a high defect concentration when x = 0.015 and maintains a relatively ordered arrangement of defect dipoles, reflecting stable local electric field distribution [41].

To objectively evaluate the variation of defect dipole concentration with KT content, baseline correction was performed on the EPR spectrum and the corresponding Y value (the plateau of the double-integrated curve) which is proportional to the relative spin concentration was obtained by quadratic integration [47], as shown in Figs. S1(c)–S1(i) in the ESM. At the $g \approx 4.23$ signal, the addition of KT reduces the full width at half maximum (FWHM) of the first-integrated curve (absorption spectrum), indicating a more homogeneous local lattice environment around the defect dipoles [48]. This facilitates the formation of a relatively ordered alignment of defect dipoles, maintaining a stable local electric field distribution. In contrast, the FWHM at the $g \approx 2.16$ signal broadens with increasing KT content, which may be related to the enhanced dipole–dipole interaction caused by the increased concentration of this type of paramagnetic center [49]. Furthermore, the Y values of the double-integrated curves at both the $g \approx 4.23$ and $g \approx 2.16$ signals increase with increasing KT content, showing the same trend, further confirming that the introduction of KT promotes the increase in defect concentration. The XPS spectra of the undoped BF–BT ceramic (Figs. S2(a)–S2(d) in the ESM) confirm the presence of Fe^{3+}, Ti^{4+}, Mn^{2+}, and $V_O^{\cdot\cdot}$, which provides the basis for the formation of $(Fe_{Ti}^{'}–V_O^{\cdot\cdot})^{\bullet}$ and $(Mn_{Ti}^{''}–V_O^{\cdot\cdot})^{\times}$ defect dipoles. Meanwhile, the oxygen vacancy concentration increases with increasing KT content (Figs. S2(d)–S2(f) in the ESM), which further confirms the enhancement of defect dipole concentration. These results provide strong support for the aforementioned EPR analysis. On the other hand, the intensity ratio I(E–7)/I(A_1–4) can be used to

Just Accepted

characterize the distortion degree of BO_6 octahedron, as shown in Fig. 2(c). The ratio first increases and then decreases with increasing x, reaching the maximum when $x = 0.015$, indicating that the lattice distortion of BO_6 octahedron is most pronounced at this composition [50]. For BF–BT-based ceramics, the enhancement in BO_6 octahedral distortion is closely associated with the increase in the R phase content [36,50], as illustrated in Fig. 2(d). Overall, the BF–BT–0.015KT sample exhibits a high concentration of defect dipoles with an ordered orientation, which is beneficial for enhancing the strain performance.

To further corroborate the underlying mechanism from the microstructure level, the surface morphology of BF–BT–xKT ceramics was characterized and the corresponding grain size distributions are presented in Fig. S3 in the ESM. At $x = 0.000$, the sample surface exhibits an uneven grain size distribution, and distinct pores are observed. With the increasing x, the grains in all samples become densely packed and uniformly distributed, demonstrating that the addition of KT promotes the densification of BF–BT-based ceramics. In addition, the average grain size shows a decreasing trend, reaching a minimum of 2.54 μm at $x = 0.015$. Generally, fine and uniformly distributed grains possess a higher grain boundary density, which is beneficial for relieving the stress focusing at grain boundaries and facilitating domain switching during poling [51]. The grain boundary density of the BF–BT–xKT ceramics can be obtained using classical stereological method [52,53], and the calculation procedure is presented in Eq. (1) (the corresponding results are given via Table S2 and Fig. S4 in the ESM).

$$S_V = \frac{2N}{L_t} \tag{1}$$

where S_v is the grain boundary density (grain boundary area per unit volume), N is the number of intersection points between the test line and the grain boundaries, and L_t is the actual length of the test line. As listed in Table S2 in the ESM, the grain boundary density reaches a maximum of 1.27 μm^{-1} at $x = 0.015$. It is worth noting that a pronounced difference in dielectric properties typically exists between the grain boundary region and the grain interior in polycrystalline ceramics [54,55]. This

Just Accepted

difference induces a non-uniform local electric field near the grain boundaries, giving rise to an electric field gradient [56]. Concurrently, small grains and dense grain boundaries may amplify this process [56]. Nevertheless, the electric field gradient generated at the microscopic level of the material is usually much lower than that generated at the macroscopic electrode edges.

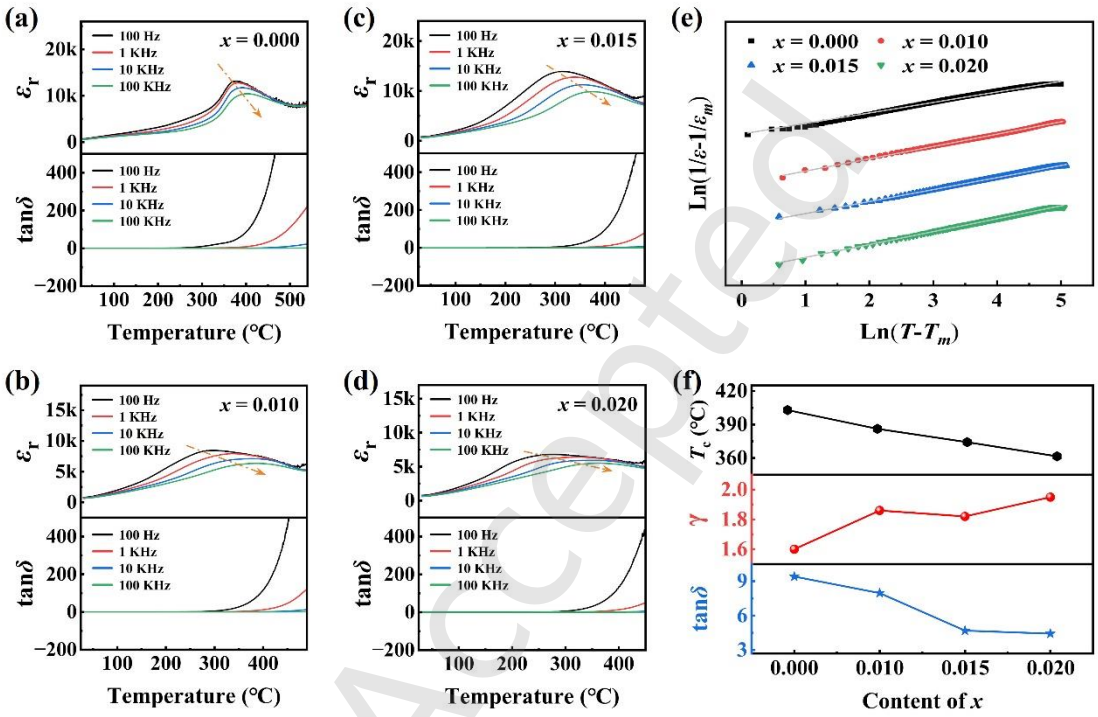

Fig. 3 (a–d) The temperature-dependent curves of ε_r and tanδ in BF–BT–xKT ceramics. (e) Dispersion index of BF–BT–xKT ceramics. (f) The variations of T_c, γ, and tanδ with respect to x in BF–BT–xKT ceramics.

Figures 3(a)–3(d) present the temperature-dependent relative dielectric constant (ε_r) and dielectric loss (tanδ) for the BF–BT–xKT ceramics. With the introduction of KT into the BF–BT ceramics, the Curie temperature (T_c) decreases from 402.9 °C to 361.5 °C. Conversely, the critical temperature at which tanδ rises sharply at high temperatures increases with increasing x, suggesting that the addition of KT effectively suppresses high-temperature leakage current, thereby enhancing the resistivity and thermal stability of the ceramics [57]. As illustrated in Fig. 3(f), the tanδ at T_c significantly decreases from 9.4 to 4.6 when x increases from 0.000 to 0.015, while a relatively high T_c of 374 °C is maintained, further confirming the improvement in high-temperature insulation performance. Temperature-dependent impedance properties provide a more intuitive evaluation of the high-temperature insulation

Just Accepted

performance in BF–BT–*x*KT ceramics, as shown in Fig. S5 in the ESM. The DC resistance (R_{dc}) was estimated from the intercept of the Nyquist plot on the real axis (Z'), based on which the corresponding DC conductivity (σ_{dc}) was calculated [58]. It can be observed that the BF–BT–0.015KT ceramic exhibits a significantly higher R_{dc} and a lower σ_{dc} compared to the undoped BF–BT ceramic over the high-temperature range of 400–500 °C, demonstrating that the introduction of KT effectively suppresses the high-temperature leakage current and improves the high-temperature resistivity of the BF–BT ceramics. Notably, as the measurement frequency increases, the dielectric peak gradually flattens and broadens, and its maximum shifts toward higher temperatures, showing pronounced frequency dispersion behavior. Such frequency dispersion is a typical characteristic of relaxor ferroelectrics, closely related to the dynamic response of polar nanoregions (PNRs) [59]. The dispersion factor (γ) which is commonly used to quantify the degree of relaxor can be obtained by fitting the dielectric temperature spectra based on the modified Curie–Weiss law (Eq. (2)) [60], and the results are shown in Figs. 3(e) and 3(f).

$$\frac{1}{\varepsilon}-\frac{1}{\varepsilon_{m}}=\frac{\left(T-T_{m}\right)^{\gamma}}{C} \tag{2}$$

where ε_m and T_m are the maximum dielectric constant and the corresponding temperature, respectively. T and ε refer to the temperature above T_m and the corresponding dielectric constant, respectively. C is a constant. It should be noted that the fitting temperature range is 50–100 °C above T_m. Additionally, the fitted γ and T_c with error bars are separately provided in Fig. S6(a) in the ESM. The value of γ ranges between 1 and 2, where $\gamma = 1$ corresponds to a normal ferroelectric and $\gamma = 2$ stands for an ideal relaxor ferroelectric. As seen from Fig. 3(f), the value of γ increases from 1.60 at $x = 0.000$ to 1.95 at $x = 0.020$, demonstrating that the addition of KT significantly enhances the relaxor properties of the BF–BT ceramics. Moreover, the ceramic exhibits a high γ of 1.82 when $x = 0.015$, which is slightly lower than that at $x = 0.020$. For BF–BT–*x*KT ceramics, the introduction of KT component induces the replacement of A-site and B-site ions by K^+ and Ta^{5+} ions, respectively. This will cause the inhomogeneity of local components, destroy the long-range ferroelectric order, and promote the

Just Accepted

formation of PNRs, thereby leading to the enhanced relaxor characteristics [61]. Characterized by small size and strong responsiveness, PNRs can contribute large strain under an external electric field [61,62]. However, the excessively strong relaxor properties with γ of 1.95 at $x = 0.020$ may render the PNRs overly active, which compromises the cooperativity and reversibility of domain switching, ultimately reducing the strain performance [63,64]. Therefore, the optimized BF–BT–0.015KT ceramic with moderate relaxor characteristics ($\gamma = 1.82$) can effectively enhance the strain response of BF–BT-based ceramics.

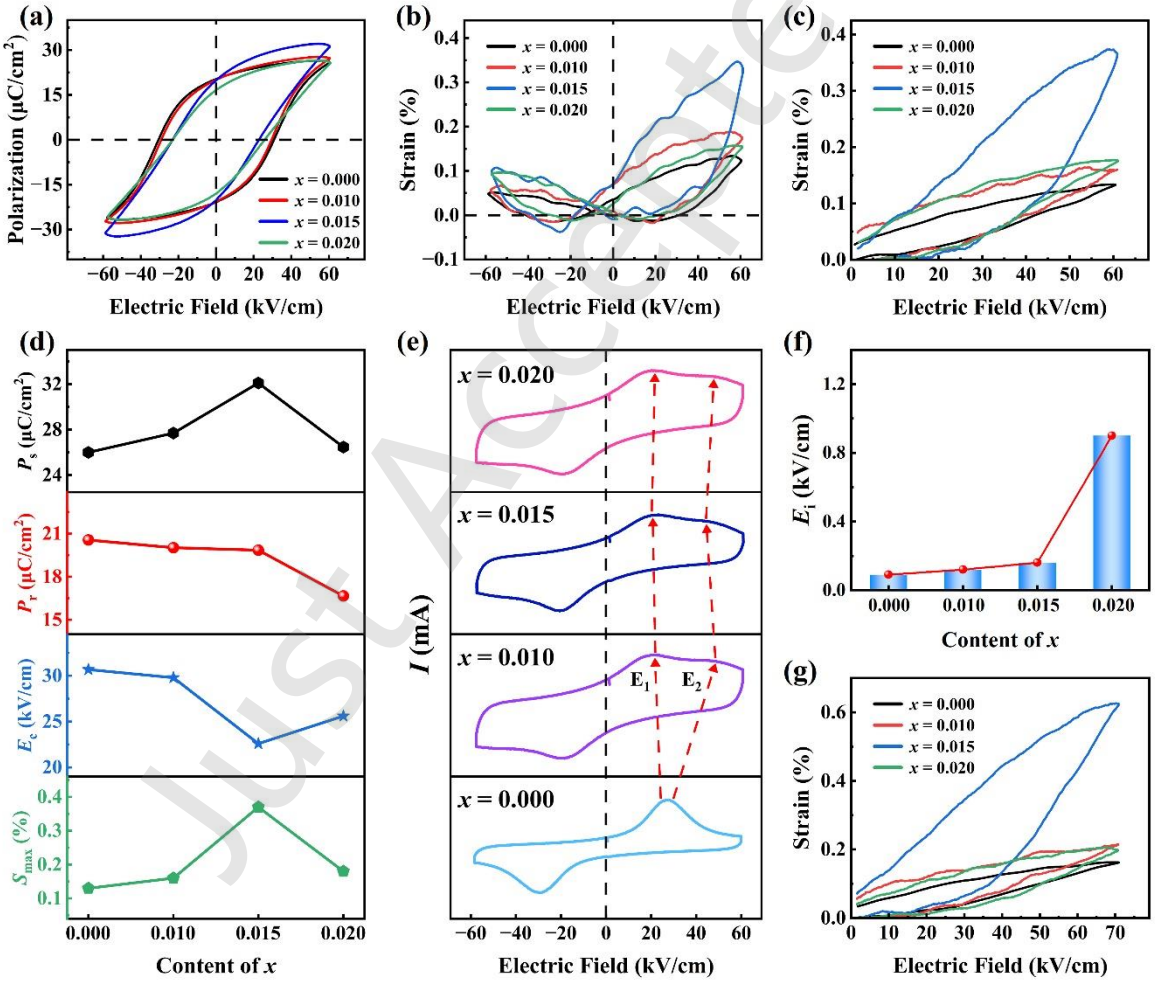

Fig. 4 BF–BT–xKT ceramics at $E = 60$ kV/cm, $t = 0.15$ mm and $r = 3$ mm: (a) P–E hysteresis loops; (b) bipolar strain curves; (c) unipolar strain curves; (d) the variations of P_s, P_r, E_c, and S_{max} with various x; (e) I–E curves; (f) the variation of E_i with KT content. (g) unipolar strain curves in BF–BT–xKT ceramics at $E = 70$ kV/cm, $t = 0.15$ mm and $r = 3$ mm.

Just Accepted

Figures 4(a)–4(c) illustrate the polarization–electric field (*P*–*E*) hysteresis loops, bipolar and unipolar strain curves of BF–BT–*x*KT ceramics. It can be observed that the addition of KT causes the *P*–*E* loops to become elongated, indicating the enhanced relaxor behavior. Meanwhile, the pronounced asymmetry observed in the bipolar strain curves is usually related to the internal bias field (E_i) induced by defect dipoles, as well as the elastic effect arising from these defect dipoles themselves [65]. In addition, the unipolar strain is significantly enhanced with increasing KT content and reaches a maximum at x = 0.015, as shown in Fig. 4(c). Figure 4(d) displays the variations of saturation polarization (P_s), remanent polarization (P_r), coercive field (E_c), and maximum unipolar strain (S_{max}) with increasing x, offering an intuitive overview of the influence of KT content on the electrical properties of BF–BT-based ceramics. For clarity, the variation of S_{max} with error bars are provided in Fig. S6(b) in the ESM. It can be found that P_s increases from 26.00 μC/cm^2 at x = 0.000 to 32.10 μC/cm^2 at x = 0.015, while P_r and E_c decrease from 20.56 μC/cm^2 and 30.67 kV/cm to 19.85 μC/cm^2 and 22.59 kV/cm, respectively. The introduction of KT component could generate a certain number of defects that promote domain switching and polarization saturation, leading to the increment of P_s. Moreover, when the direction of applied electric field is the same as the internal bias field, the effective driving electric field is enhanced, resulting in a reduction in E_c. Simultaneously, the macroscopic internal bias field can provide a restoring force for domain switching, enabling more domains to revert to their initial state upon removal of the external electric field, which consequently lowers P_r. However, when x = 0.020, excessive defect concentration can promote the association or aggregation of adjacent charged defects, forming composite defect dipoles such as Fe'_{Ti}–$V_O^{\cdot\cdot}$–Fe'_{Ti} and significantly enhancing the internal bias field [65]. The change of E_i calculated from the positive and negative coercive electric fields with respect to KT content is shown in Fig. 4(f), confirming the enhancement of E_i [62]. This enhanced internal bias field is accompanied by a strong pinning effect that suppresses domain switching and polarization saturation, thereby resulting in a decrease of P_s and an increase of E_c. Meanwhile, the excessively strong relaxor characteristics enable the electric domains to quickly revert

Just Accepted

toward their original state even after the external electric field is removed, resulting in a continuous decrease of P_r. Figures S7(a)–S7(h) in the ESM display the bipolar and unipolar strain curves of BF–BT–xKT ceramics at different thicknesses, and the S_{max} with error bars for different thicknesses are summarized in Fig. S6(c) in the ESM. One can observe that the strain greatly increases with the decrease of thickness. According to Fig. S7(i) in the ESM, the S_{max} reaches the maximum at x = 0.015 and t = 0.15 mm, and its corresponding bipolar strain curve (Fig. S7(e) in the ESM) also exhibits the greatest asymmetry. This indicates that the defect dipoles of this composition (x = 0.015) display the strongest effect on enhancing strain. Combined with the previous Raman results, it can be concluded that the BF–BT–0.015KT ceramic locates within the optimal defect dipole concentration window (a higher defect dipole concentration and a greater degree of orientation ordering).

Figure 4(e) shows the current–electric field (I–E) curves of the BF–BT–xKT ceramics. The undoped sample exhibits a single and sharp current peak, which is attributed to the switching of ferroelectric macro-domains [66]. However, this single current peak evolves into two distinct peaks E_1 and E_2 when KT is introduced into the BF–BT ceramics, indicating the presence of nano-domains. Under an applied electric field, the domain structure undergoes two sequential processes: the transformation of nano-domains into ferroelectric macro-domains and the directional switching of those ferroelectric macro-domains, corresponding to current peaks E_1 and E_2, respectively [11]. Moreover, the current peak E_1 shifts toward lower electric fields with increasing KT content, revealing a reduced switching barrier for the nano-domains, which is consistent with the decrease in E_c observed in the P–E hysteresis loops. Figure 4(g) displays the unipolar strain curves of BF–BT–xKT ceramics measured at 70 kV/cm, and the trend is consistent with that observed at 60 kV/cm. The S_{max} with error bars at both 60 kV/cm and 70 kV/cm are provided in Fig. S6(b) in the ESM. Excitingly, the BF–BT–0.015KT ceramic with a thickness of 0.15 mm and electrode radius of 3 mm achieves a high strain of 0.62% at 70 kV/cm.

Just Accepted

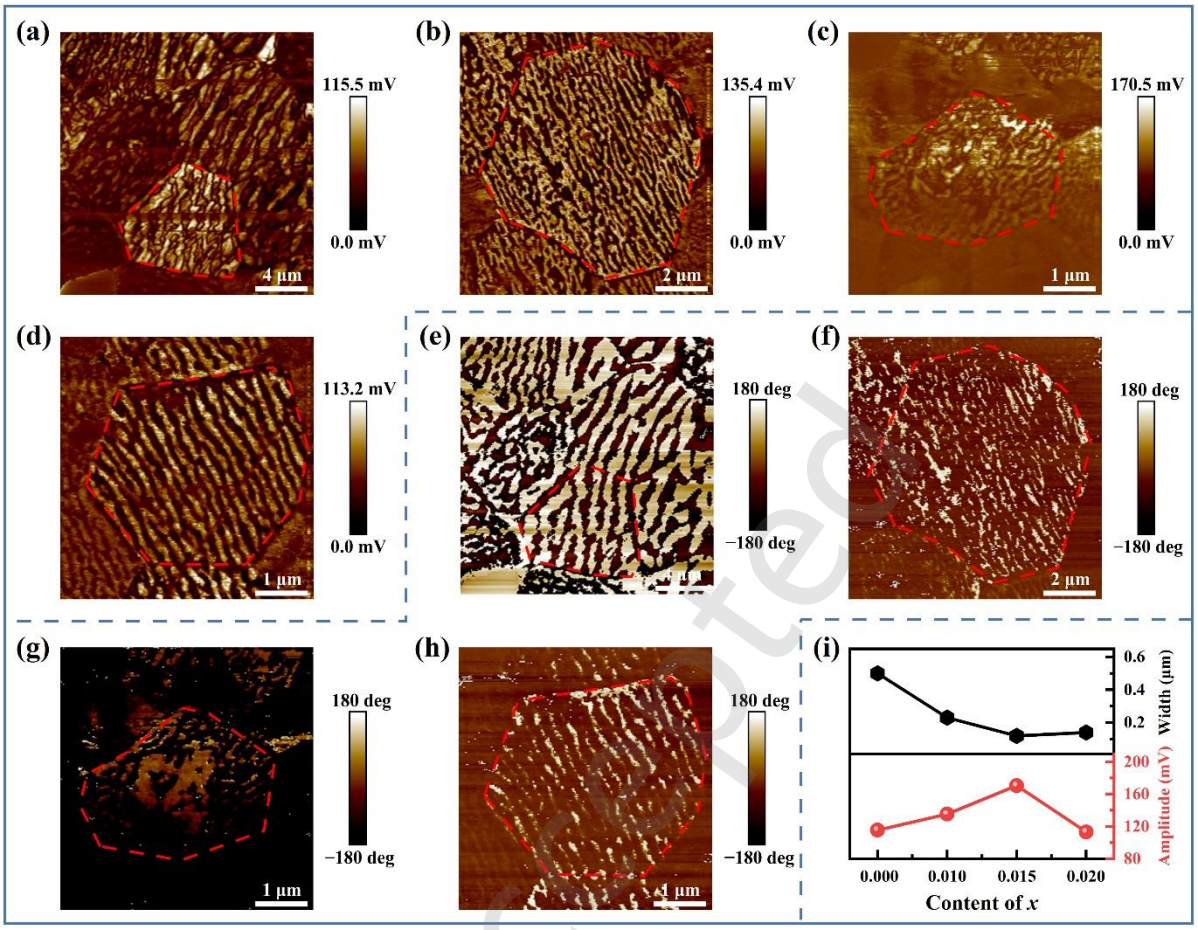

Fig. 5 PFM amplitude images of BF–BT–*x*KT ceramics for (a) $x = 0.000$, (b) $x = 0.010$, (c) $x = 0.015$, and (d) $x = 0.020$. PFM phase images of BF–BT–*x*KT ceramics for (e) $x = 0.000$, (f) $x = 0.010$, (g) $x = 0.015$, and (h) $x = 0.020$. (i) The variation of domain width and amplitude as increasing x in BF–BT–*x*KT ceramics.

To intuitively analyze the influence of domain structure on strain properties, the amplitude and phase images of BF–BT–*x*KT ceramics were measured using PFM, as presented in Fig. 5. The undoped sample exhibits ferroelectric macro-domains in the form of stripe or herringbone with relatively large domain size. When KT is introduced into BF–BT ceramics, the increment of the concentration of defect dipoles gradually disrupts the continuity of these ferroelectric macro-domains [67]. The domain width is significantly reduced and island-like domains appear. At $x = 0.015$, the domain width is further reduced to 0.12 μm, exhibiting typical nano-domain characteristics. The reduction in domain width directly lowers the domain switching barrier, enabling domains to respond easily under external electric fields [68]. At the same time, a unique and evenly distributed domain structure is formed where

Just Accepted

central island-like domains coexist with surrounding stripe domains. Owing to their smaller width compared to the central island-like domains, these peripheral stripe domains will respond preferentially to the applied electric field. In ferroelectrics, the preferential switching of small stripe domains induces elastic deformation of the surrounding lattice and produces localized stress fields. The generated stress fields will affect the local stress state of the central island-like domains, thereby reducing their domain switching barrier [69]. Simultaneously, the switching of stripe domains generates local strain and induces a localized electric field in their vicinity, providing an additional driving force for the switching of the central island-like domains [69]. Consequently, the preferential response of the stripe domains drives the cooperative switching of the central island-like domains, significantly enhancing the strain performance. This cooperative mechanism establishes a domain structure foundation with low energy barrier, rapid response, and high strain output efficiency. However, at $x = 0.020$, the domain structure reverts to a continuous arrangement of stripe or herringbone domains. Although the width of the domains is still small, the synergistic effect of domain switching is weakened, leading to a decrease in the strain properties. Besides, the size of PNRs is usually around several nanometers, making them difficult to observe directly in PFM images. Nonetheless, the response activity of PNRs is closely related to the piezoelectric response strength [70]. As shown in Figs. 5(a)–5(d), the PFM amplitude increases from 115.5 mV to 170.5 mV when x changes from 0.000 to 0.015, indicating significant enhancement in the piezoelectric response activity. In contrast, the piezoelectric response is considerably reduced at $x = 0.020$. The above findings indirectly prove that moderate presence of PNRs is beneficial for enhancing the strain properties of BF–BT–xKT ceramics.

Just Accepted

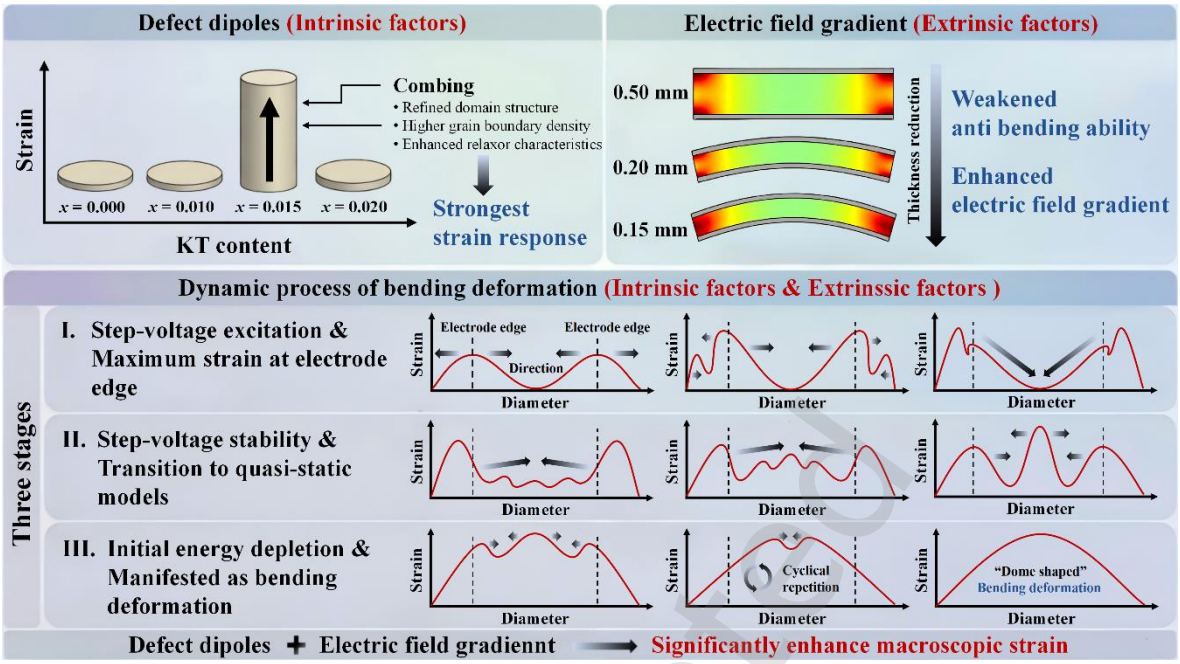

Fig. 6 Schematic diagram and dynamic bending process of BF–BT–*x*KT ceramics.

Figure 6 presents the mechanism underlying the ultrahigh strain developed in the prepared BF–BT–*x*KT ceramics. Compared to other compositions (x = 0.000, 0.010, 0.020), the ceramic with x = 0.015 lies within the optimal defect dipole concentration window, and exhibits enhanced relaxor characteristics, refined domain structures, and increased grain boundary density. These intrinsic microstructural factors collectively lead to a significantly superior strain response under identical step-voltage excitation. Meanwhile, as the sample thickness decreases, a significant electric field gradient is generated at the electrode edge, and there exists an electric field strength far greater than the nominal electric field at the center. This gradient progressively penetrates the entire sample along the thickness direction, providing a stronger driving force for non-uniform strain. It is thus clear that the synergistic effect of defect dipoles (intrinsic factors) and electric field gradient (extrinsic factors) can significantly enhance the macroscopic strain of BF–BT-based ceramics. Crucially, the bending resistance of thin samples is much lower than that of thick samples. Therefore, under the same voltage excitation, thin samples are more prone to bending deformation. On this basis, a dynamic bending deformation process was established in this study, which is divided into three stages. For Stage I, upon application of a step-voltage to the ceramic disc, the electrode edge instantaneously generates maximum strain due to the

Just Accepted

presence of electric field focusing and gradient. This instantaneous strain wave immediately propagates toward both the electrode center and the sample boundary. Upon reaching the boundary, the strain wave reflects and overlaps with the incoming strain wave, forming a new strain peak. Meanwhile, the strain amplitude decreases along the direction from the electrode edge toward the center. For Stage II, this superimposed peak migrates toward the electrode center. As the step-voltage stabilizes and continues to excite the sample, several smaller strain peaks appear in the region between the electrode edge and the center. Since the strain wave continues propagating toward the center, the original superimposed peaks continue to migrate and eventually refocus at the electrode edge. Simultaneously, the electrode center develops a unique maximum strain peak due to geometric focusing. Notably, several strain peaks that are previously located between the electrode edge and the center disappear, indicating that the bending deformation process induced by the step-voltage is beginning to transition toward a quasi-static state. Within Stage III, the superimposed strain peaks continue to migrate toward the center, while the central maximum peak spreads outward. The two wavefronts meet and overlap in the intermediate region between the electrode edge and the center, forming several larger strain peaks. This cyclic process repeats until the transient strain wave energy from the step-voltage excitation is completely exhausted. Finally, the ceramic disc exhibits a dome-shaped bending strain distribution that is high in the center and low at the edges.

Just Accepted

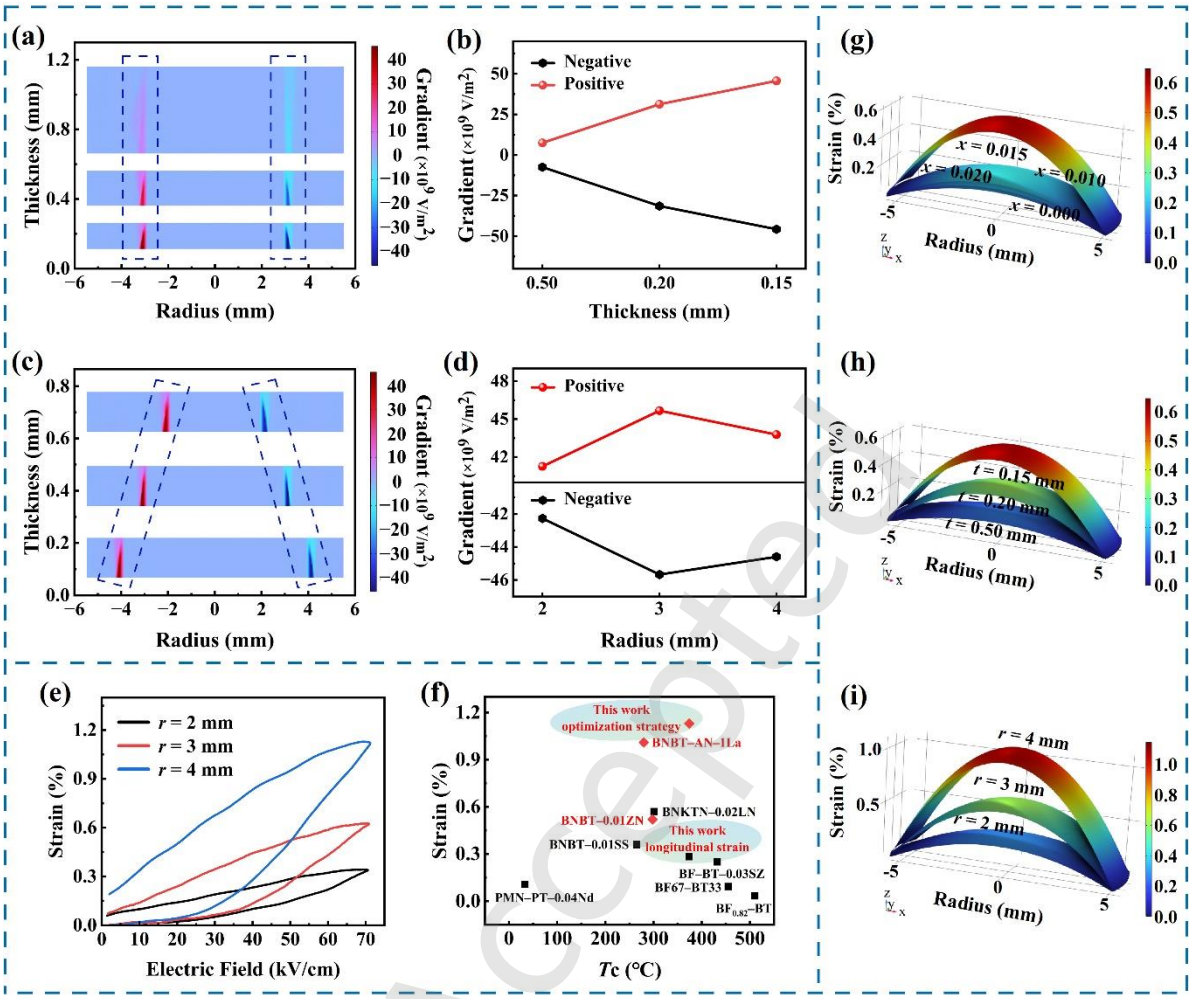

Fig. 7 Finite element analysis of electric field gradient at electrode edges in BF–BT–0.015KT ceramic under different conditions: (a, b) different thicknesses (t = 0.15, 0.20, and 0.50 mm) at r = 3 mm; (c, d) different electrode radii (r = 2, 3, and 4 mm) at t = 0.15 mm. (e) Strain curves of the BF–BT–0.015KT ceramic (t = 0.15 mm) with different electrode radii (r = 2, 3, and 4 mm) from experimental testing. (f) Performance comparison (square: true longitudinal strain, and diamond: bending deformation) between this work and other reported systems. Finite element analysis of strain sections in BF–BT–xKT ceramics under different conditions: (g) different components (x = 0.000, 0.010, 0.015, and 0.020) at t = 0.15 mm and r = 3 mm; (h) different thicknesses (t = 0.15, 0.20, and 0.50 mm) at x = 0.015 and r = 3 mm; (i) different electrode radii (r = 2, 3, and 4 mm) at x = 0.015 and t = 0.15 mm.

To verify the aforementioned dynamic bending process and its influencing factors, a finite element model composed of BF–BT–xKT ceramics, electrode, and substrate was established (Fig. S8 in the ESM). Constraints were applied to the substrate, which serves only for force transmission. In the finite

Just Accepted

element analysis, the Jiles–Atherton (*J–A*) model [71] was employed to describe the polarization hysteresis behavior of BF–BT ceramics. The coupling with ferroelectroelasticity further characterizes the electric field-induced strain response. It should be noted that the parameters describing the *J–A* model are phenomenological, including the domain wall density (a), pinning loss (k), interdomain coupling (α), polarization reversibility (c), and saturation polarization (P_s). Accordingly, the model parameters (Table S3 in the ESM) of BF–BT–xKT ceramics were calibrated by fitting the experimentally measured *P–E* hysteresis loops (Fig. S9 in the ESM), where P_s is the experimentally measured polarization value of BF–BT–xKT ceramics. Moreover, the additional polarization contributed by the oriented alignment of defect dipoles, along with its synergistic effect on domain switching, was equivalently simulated through applying an additional bias electric field to reduce the internal complexity of the model. The response time of defect dipoles under an external electric field is much shorter than the strain measurement time, so they can be approximated as a stable bias electric field. Meanwhile, the influence of defect dipoles on the synergistic effect of domain switching can also be compensated by an additional bias electric field. On this basis, the effective driving field (the contribution of the applied electric field and the bias electric field equivalent to the defect dipole effect, E_{eff}) of BF–BT–0.015KT ceramic was taken as the benchmark. The E_{eff} of the other compositions were calibrated based on the asymmetry degree of bipolar strain and the influence mechanism of defect dipoles. The E_{eff} (Table S3 in the ESM) of BF–BT–xKT ceramics is 0.51E_{eff} (x = 0.000), 0.76E_{eff} (x = 0.010), E_{eff} (x = 0.015), and 0.74E_{eff} (x = 0.020), respectively. Although the pinning effect and relaxation process of defect dipoles are not explicitly considered, the simulated strain results and trends under different compositions and thicknesses presented below are close to those of the experiments, indicating that this equivalent treatment is reasonable for macroscopic strain analysis. The convergence of the steady-state and transient finite element simulations also confirms the accuracy and reliability of the model, as shown in Fig. S10 in the ESM. Figures 7(a) and 7(b) display the electric field gradient at the electrode edge for ceramics (x = 0.015 and r = 3 mm) with different thicknesses. A significant

Just Accepted

electric field gradient is clearly visible at the edge, which increases by approximately one order of magnitude with decreasing thickness. Figure S11 in the ESM further confirms that the electric field distribution at the electrode edge is uneven, and there exists an electric field strength far greater than the nominal electric field at the center. Figure 7(g) illustrates the strain sections (the overall distribution is presented in Fig. S13 in the ESM) of the BF–BT–xKT ceramics (t = 0.15 mm and r = 3) with different compositions. When x increases to 0.015, the ceramic achieves an ultrahigh strain of 0.63%. Figure 7(h) presents the strain sections (the overall distribution is presented in Fig. S13 in the ESM) for varying thickness at this optimal composition. One can observe that the strain significantly decreases to 0.06% as the thickness increases from 0.15 mm to 0.50 mm. Figures S12(a)–S12(c) in the ESM provide the strain sections of other components with varying thicknesses. All samples exhibit the same evolution trend. However, for other compositions, the decrease of the thickness does not yield significant strain enhancement. Therefore, the ultrahigh strain for the samples is obtained only at x = 0.015 and t = 0.15 mm, far exceeding the values under other conditions. This substantiates that the ultrahigh strain originates from the synergistic optimization of defect dipoles (intrinsic factors) and the electric field gradient (extrinsic factors).

Given that the electric field gradient originates at the electrode edge and the bending strain is closely related to the factors such as disc radius, the electric field strength, and sample thickness. Therefore, the influence of electrode radius on the electric field gradient and bending strain of BF–BT–xKT ceramics was further investigated. Figures 7(c) and 7(d) present the electric field gradient at the electrode edge for ceramics (x = 0.015 and t = 0.15 mm) with different electrode radii. The gradient reaches maximum when r = 3 mm and remains relatively insensitive to the changes of electrode radii. Figure 7(i) shows the strain sections (the overall distribution is shown in Fig. S14 in the ESM) of the BF–BT–0.015KT ceramic (t = 0.15 mm) with different electrode radii. When r increases from 2 mm to 4 mm, the strain significantly increases from 0.29% to 1.12%. Although the electric field gradient is slightly smaller at r = 4 mm compared to r = 3 mm, the effective electrode area contributing to strain

Just Accepted

generation is significantly larger. Thus, the sample achieves an ultrahigh strain of 1.12% under this condition. The strain sections of other components at different radii supplemented by Figs. S12(d)–S12(f) in the ESM also demonstrate that the increasing electrode radius leads to varying degrees of strain enhancement. Figure 7(e) provides the experimentally measured strain curves of the BF–BT–0.015KT ceramics (t = 0.15 mm) with different electrode radii (r = 2, 3, and 4 mm) at 70 kV/cm, and the S_{max} with error bars for different electrode radii are presented in Fig. S6(d) in the ESM. It can be seen that the strain increases from 0.34% to 1.13% as the electrode radius increases from 2 mm to 4 mm, which is in excellent agreement with the simulation results, confirming the reliability and accuracy of the model developed in this work. Figure 7(f) presents the performance comparison between this work and recently reported representative piezoelectric ceramics [4,62,72–77], where square and diamond denote true longitudinal strain and bending deformation, respectively. The detailed performance indicators and test conditions for each data point are listed in Table S4. It can be observed that the true longitudinal strain (S_{max} = 0.28% in Fig. S15(b) in the ESM) of BF–BT–0.015KT ceramic (t = 0.40 mm and full-electrode) with a high Curie temperature (T_c = 374 °C) is comparable to other reported systems. Notably, through the synergistic optimization of defect dipoles and electric field gradient, an ultrahigh strain of 1.13% is achieved in BF–BT–0.015KT ceramic (t = 0.15 mm and r = 4 mm), outperforming most reported bending deformation systems. Furthermore, the contribution of longitudinal strain and bending strain were distinguished in BF–BT–0.015KT ceramic (t = 0.15 mm and r = 4 mm) using a small-sized sample (t = 0.15 mm and r = 0.4 mm) with full-electrode [3,4], as shown in Fig. S15(a) in the ESM. Because the small-sized sample exhibits a large ratio of thickness to diameter and the test fixture is larger than the sample, the bending effect is significantly suppressed. Meanwhile, the full-electrode configuration effectively reduces the electric field gradient, which further inhibits the bending effect. Therefore, the strain of a small-sized sample with a full-electrode can be considered as the longitudinal strain. As shown in Fig. S15(b), the measured longitudinal strain of BF–BT–0.015KT ceramic under small-sized (t = 0.15 mm and r = 0.4 mm) and full-electrode

Just Accepted

conditions is 0.32% (red curve), while the BF–BT–0.015KT ceramic (t = 0.15 mm and r = 4 mm) exhibits the total strain of 1.13% (blue curve), which consists of 0.32% longitudinal strain and 0.81% bending strain, indicating that the bending strain contributes approximately 71.68% of the total measured strain. The cyclic stability and thermostability of the unipolar strain in the BF–BT–0.015KT ceramic (t = 0.15 mm and r = 4 mm) are provided in Figs. S15(c) and S15(d) in the ESM. It can be found that the unipolar strain degrades by 7.9% after 4×10^5 cycles and changes by 8.3% within the temperature range of 25–150 ℃. Overall, the BF–BT–0.015KT ceramic (t = 0.15 mm and r = 4 mm) achieves an ultrahigh strain (S_{max} = 1.13%) while simultaneously maintaining a high Curie temperature (T_c = 374 ℃), excellent cyclic stability (4×10^5 cycles, degrades by 7.9%), and good thermostability (25–150 ℃, varies by 8.3%), demonstrating its great potential as a lead-free piezoelectric material for bending actuator applications.

$$V_t = V_0\left(1-\exp^{-\tau/(1\times10^{-6})}\right) \tag{3}$$

Based on steady-state results, a transient analysis was conducted to describe the dynamic process of bending deformation. The step-voltage during transient process is defined by Eq. (3). According to the engineering practice, the step-voltage is considered to reach the target value and remain stable when τ exceeds 5×10^{-6} s. Figures 8(a)–8(c) illustrate the three stages of dynamic bending strain of the ceramics (x = 0.015, t = 0.15 mm, and r = 4 mm). Stage I: After applying a step-voltage, the highest strain peak preferentially appears at the electrode edge and migrates to both sides over time; Stage II: The step-voltage tends to stabilize and the model gradually transitions to quasi-static state. Significant strain peaks appear at the center of the electrode due to the geometric focusing; Stage III: The strain peak in the central region spreads outward, while the strain peak at the electrode edge continues to migrate toward the center, ultimately forming a curved shape resembling a “dome”. The strain distribution (Fig. S16 in the ESM) visually demonstrates this dynamic transmission process. In addition, Fig. S17 in the ESM supplements the dynamic bending process for other compositions (t = 0.15 mm and r = 3 mm), which is consistent with the above description. The time-dependent strain amplitude at the electrode

Just Accepted

edge for the ceramics (t = 0.15 mm and r = 3 mm) with different compositions is extracted and shown in Fig. 8(e). When x = 0.015, the strain growth rate is much higher than that of the other compositions, indicating that BF–BT–0.015KT ceramic exhibits the strongest strain response at the electrode edge. Similarly, Fig. 8(d) displays the strain amplitude of the ceramics (x = 0.015 and r = 3 mm) with different thicknesses as a function of time. It can be seen that reducing the sample thickness can significantly enhance the strain response at the electrode edge. When t = 0.50 mm, the ceramic quickly reaches its steady-state maximum strain, followed by extremely slow strain growth, implying that the thick samples possess considerably higher bending resistance. When the thickness decreases to 0.20 mm, the strain continues to increase rapidly even after reaching steady-state. This is because the constraints are imposed only on the lower surface of the substrate. Theoretically, piezoelectric ceramics could undergo unlimited strain wave propagation under step-voltage excitation. Nevertheless, the rigid constraints of the ceramic practically limit the number of strain wave cycles during Stage III. Figure S18 in the ESM supplements the dynamic bending process of the ceramics (x = 0.015 and r = 3 mm) with different thicknesses. When t = 0.50 mm, the propagation of the strain wave is obstructed, while when t = 0.20 mm, the propagation process is similar to that at t = 0.15 mm. This confirms that the bending resistance is significantly enhanced with increasing thickness. Accordingly, the strain response induced by a single excitation is relatively weak in the samples, and multiple excitations are required during Stage III to reach their steady-state strain.

Figure 8(f) presents the strain amplitude at center point of the ceramics (x = 0.015 and t = 0.15 mm) with different electrode radii. The strain response is significantly enhanced with increasing electrode radius. Moreover, slight variations in the strain wave propagation process are observed among different radii (Fig. S19 in the ESM). In the process of Stage II, the time required for the strain peak of the ceramic with large radius to re-aggregate at the electrode edge decreases. Subsequently, the strain amplitude is significantly higher than that of ceramics with small radii under electrode edge excitation. It is worth noting that the dynamic bending process of the BF–BT–xKT ceramics at r = 2 mm is

Just Accepted

significantly different from those at larger radii. In Stage II, the strain peak does not re-aggregate at the electrode edge. This is because the transmission time of strain wave from the electrode edge to the central region is much shorter than the time to the sample boundary, so the geometric focusing effect induces significant strain at the center more rapidly. Consequently, the bending deformation process enters Stage III before the strain wave reaches the electrode edge. Meanwhile, the reduction of electrode radius significantly decreases the strain excitation area, leading to a sharp decrease in overall strain. Therefore, in order to reach its steady-state strain, multiple cyclic excitations are also required in Stage III.

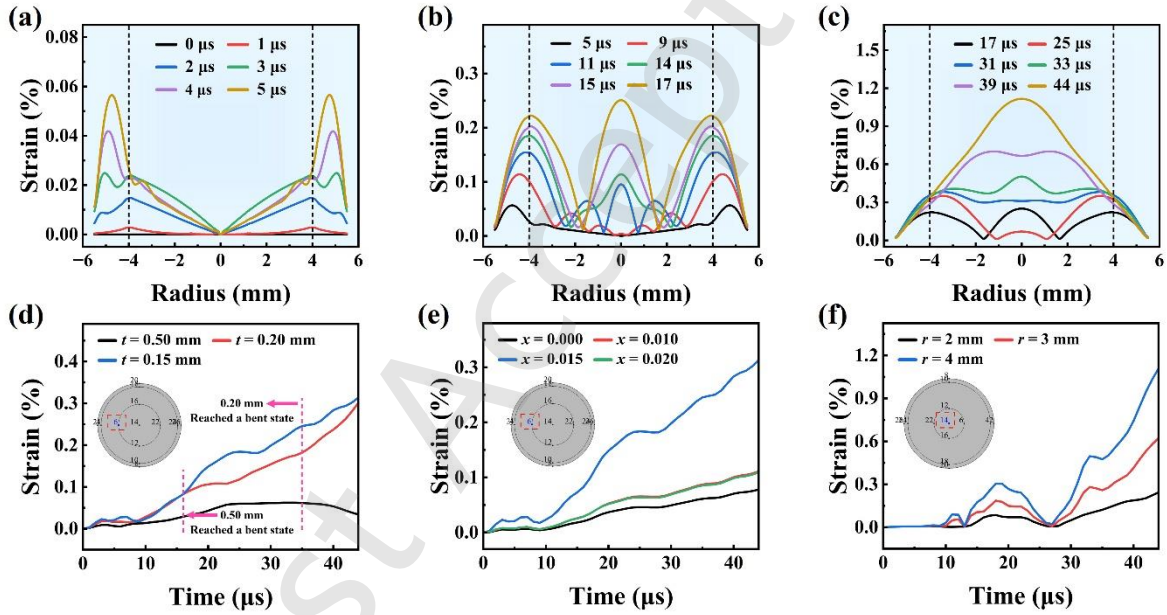

Fig. 8 Finite element analysis of BF–BT–*x*KT ceramics: dynamic bending process at $x = 0.015$, $t = 0.15$ mm, and $r = 4$ mm for (a) Stage I, (b) Stage II, and (c) Stage III; (d) strain response of the ceramics ($x = 0.015$ and $r = 3$ mm) at the electrode edges with different thicknesses ($t = 0.50$, 0.20, and 0.15 mm); (e) strain response of the ceramics ($t = 0.15$ mm and $r = 3$ mm) at the electrode edges with different compositions ($x = 0.000$, 0.010, 0.015, and 0.020); (f) strain response of the ceramics ($x = 0.015$ and $t = 0.15$ mm) at the electrode center with different radii ($r = 2$, 3, and 4 mm).

Just Accepted

4 Conclusions

In this study, BF–BT–*x*KT piezoelectric ceramics were prepared, and a new strategy for synergistically enhancing strain through defect dipoles (intrinsic factors) and electric field gradient (extrinsic factors) was proposed. The BF–BT–0.015KT ceramic exhibits an optimal defect dipole concentration, enhanced relaxor characteristics, and refined domain structure, and these optimized intrinsic material properties effectively amplify the contribution of the electric field gradient in enhancing the strain response and promoting domain switching of the materials. Finite element analysis confirms that the electric field gradient at electrode edges in thin samples is approximately one order of magnitude higher than in thick samples, providing stronger extrinsic driving force for bending deformation. Meanwhile, the dynamic bending process is visually revealed. Under the synergistic optimization of defect dipoles and electric field gradient, the BF–BT–0.015KT ceramic (t = 0.15 mm and r = 4 mm) achieves an ultrahigh strain of 1.13%, while maintaining a high Curie temperature (T_c = 374 °C), excellent cyclic stability (4×10^5 cycles, degrades by 7.9%), and good thermostability (25–150 °C, varies by 8.3%). These findings provide novel insights for the development of high-performance lead-free piezoelectric materials for bending actuator applications.

Acknowledgements

This work was financially supported by the National Natural Science Foundation of China (No. 62371366), the Central Government-Guided Local Science and Technology Development Special Project of Ningxia Hui Autonomous Region (No. 2026FRE05019), the Fundamental Research Funds for the Central Universities and the Postgraduate Innovation Fund of Xidian University (YJSJ26019). We also acknowledge the Instrumental Analysis Center of Xidian University for providing test equipment.

Just Accepted

Author contributions

Huangtao Wu: Writing - review & editing, Writing - original draft, Methodology, Investigation, Formal analysis, Data curation. **Zhibo Chen:** Investigation, Data curation. **Jinbo Zhao:** Investigation, Methodology. **Zhen Zhang:** Validation, Data curation. **Hongyu Yang:** Supervision, Investigation; **Linzhuang Xing:** Writing - review & editing, Project administration. **Zhimin Li:** Writing - review & editing, Supervision, Resources, Funding acquisition.

Availability of data and materials

The data that support the findings of this study are available from the corresponding author upon reasonable request.

Competing interests

The authors have no competing interests to declare that are relevant to the content of this article.

Electronic Supplementary Material (ESM)

Supplementary material above is available in the online version of this article.

References

[1] Jin HN, Gao XY, Ren KL, *et al.* Review on piezoelectric actuators based on high-performance piezoelectric materials. *IEEE Trans Ultrason Ferroelectr Freq Control* 2022, **69**: 3057–3069.

[2] Jiang DH, Luo F, Pei K, *et al.* Realizing large strain at low electric field in Pb(Zr,Ti)O_3-based piezoelectric ceramics via engineering lattice distortion and domain structure. *J Adv Ceram* 2024, **13**: 1409–1421.

[3] Wang J, Wang BQ, Zhang HJ, *et al.* Ultrahigh electrobending deformation in lead-free piezoelectric ceramics via defect concentration gradient design. *Adv Mater* 2024, **36**: 2404682.

[4] Jia YX, Fan YB, Lei L, *et al.* Ultrahigh electrobending deformation in poled sodium bismuth titanate-based piezoelectric ceramics by uneven defect distribution. *Adv Funct Mater* 2025, **35**: 2421320.

Just Accepted

[5] Wu JG, Gao XY, Chen JG, *et al.* Review of high temperature piezoelectric materials, devices, and applications. *Acta Phys Sin* 2018, **67**: 207701

[6] Balaram V, Rambabu U, Reddy MRP, *et al.* RoHS regulation: challenges in the measurement of substances of concern in industrial products by different analytical techniques. *Mapan* 2018, **33**: 329–346.

[7] Li HT, Zhao JW, Li Y, *et al.* Bismuth ferrite-based lead-free high-entropy piezoelectric ceramics. *ACS Appl Mater Interfaces* 2024, **16**: 9078–9087.

[8] Chen Y, Zhou Z, Li LF, *et al.* Synergistically enhancing the piezoelectric activity and Curie temperature of $CaBi_4Ti_4O_{15}$ ceramics via co-doping Gd/Mn at the A/B-site. *J Adv Ceram* 2024, **13**: 1482–1497.

[9] Tittmann BR, Batista CFG, Trivedi YP, *et al.* State-of-the-art and practical guide to ultrasonic transducers for harsh environments including temperatures above 2120 °F (1000 ℃) and neutron flux above 10^{13} n/cm^2. *Sensors-Basel* 2019, **19**: 4755.

[10] Yang HB, Zhu JM, Wang XT, *et al.* Significantly enhancing high-temperature piezoelectric response and T_{dr} of BF-BT-based ceramics through multi-component optimization strategy. *Chem Eng J* 2024, **498**: 154975.

[11] Zhu YH, Tan YM, Pei K, *et al.* Enhanced strain and its temperature stability in BF-BT-based piezoelectric ceramics via Hf modification. *Ceram Int* 2025, **51**: 29499–29509.

[12] Zhang SY, Zhang XX, Hu JH, *et al.* Ultra-high piezoelectric properties of $BiFeO_3$–$BaTiO_3$ lead-free piezoelectric ceramics enabled by a one-step sintering process. *J Adv Ceram* 2026, **15**: 9221302.

[13] Yuan J, Ruan TT, Li Q, *et al.* Large strain and reduced hysteresis of $BiFeO_3$-$x$$BaTiO_3$ lead-free ceramic via multiphase coexistence and relaxor behaviors. *Ceram Int* 2022, **48**: 26335–26341.

[14] Peng JG, Liu WB, Zeng JT, *et al.* Large electromechanical strain at high temperatures of novel <001> textured $BiFeGaO_3$-$BaTiO_3$ based ceramics. *J Mater Sci Technol* 2020, **48**: 92–99.

[15] Li B, Zheng T, Wu JG. Structural disorder and oxygen octahedron evolution via defect engineering for properties enhancement in BF–BT ceramics. *J Am Ceram Soc* 2024, **107**: 4789–4800.

[16] Zhao X, Zheng T, Liu Q, *et al.* Synergistically enhanced strain and piezoelectric properties in BNT-modified BF–BT-based ceramic. *J Am Ceram Soc* 2025, **108**: e70176.

[17] Das Adhikary G, Adukkadan A, Muleta GJ, *et al.* Longitudinal strain enhancement and bending deformations in piezoceramics. *Nature* 2025, **637**: 333–338.

[18] Hou DW, Liu XY, Li Y, *et al.* Effects of thickness and defect on ultrahigh electro strain of piezoelectric ceramics. *Ceram Int* 2024, **50**: 39918–39926.

Just Accepted

[19] He X, Boda MA, Chen C, *et al.* Ultra-large electromechanical deformation in lead-free piezoceramics at reduced thickness. *Mater Horiz* 2024, **11**: 1079–1087.

[20] Adhikary GD, Singh DN, Tina GA, *et al.* Ultrahigh electrostrain >1% in lead-free piezoceramics: role of disk dimension. *J Appl Phys* 2023, **134**: 054101.

[21] Samantaray MM, Gurav A, Dickey EC, *et al.* Electrode defects in multilayer capacitors part II: finite element analysis of local field enhancement and leakage current in three-dimensional microstructures. *J Am Ceram Soc* 2011, **95**: 264–268.

[22] Lou XH, Hou X, Chen YJ, *et al.* Electromechanical grain boundary model with formation mechanism in polycrystalline ferroelectrics. *J Appl Phys* 2022, **132**: 224105.

[23] Fridkin VM. Domains and switching in ferroelectricity. *Ferroelectrics* 2012, **426**: 139–141.

[24] Zhao JW, Funni SD, Kmet B, *et al.* Inhomogeneous domain switching near an electrode edge in orthorhombic $K_{0.5}Na_{0.5}NbO_3$ piezoceramic. *Scr Mater* 2024, **246**: 116089.

[25] Rhun GL, Vrejoiu I, Pintilie L, *et al.* Increased ferroelastic domain mobility in ferroelectric thin films and its use in nano-patterned capacitors. *Nanotechnology* 2006, **17**: 3154–3159.

[26] Wang J, Fu GH, Zhang HJ, *et al.* Asymmetric electrostrain/electrobending in piezoelectric ceramics: role of defect dipoles or oxygen vacancies. *Adv Sci* 2026: e75649.

[27] Tan Z, Lv X, Jiang LM, *et al.* Universal theoretical elucidation of electrobending deformation in piezoelectrics. *Phys Rev Lett* 2025, **134**: 226801.

[28] Yabuta H, Watanabe M, Watanabe T, *et al.* Structural investigation of ferroelectric $BiFeO_3$–$BaTiO_3$ solid solutions near the rhombohedral–pseudocubic phase boundary. *Appl Phys Lett* 2020, **116**: 252902.

[29] Tang L, Li JZ, Zhou XF, *et al.* Deciphering the high-temperature phase transitions and piezoelectric response in 75$BiFeO_3$-25$BaTiO_3$ piezoceramics. *Acta Mater* 2025, **299**: 121482.

[30] Ren ZH, Hu JX, Shi LN, *et al.* Enhanced photostrictive properties in ternary (1-*x*)(0.7$BiFe_{1-y}Mn_yO_3$-0.3$BaTiO_3$)-*x*$KTaO_3$ ceramics. *Ceram Int* 2023, **49**: 6270–6279.

[31] Shannon RD. Revised effective ionic radii and systematic studies of interatomic distances in halides and chalcogenides. *Acta Crystallogr, Sect A* 1976, **32**: 751–767.

[32] Wang B, Li YZ, Hall DA. Surface structure and quenching effects in $BiFeO_3$-$BaTiO_3$ ceramics. *J Am Ceram Soc* 2021, **105**: 1265–1275.

[33] Chen JG, Daniels JE, Jian J, *et al.* Origin of large electric-field-induced strain in pseudo-cubic $BiFeO_3$–$BaTiO_3$ ceramics. *Acta Mater* 2020, **197**: 1–9.

Just Accepted

[34] Xun BW, Wang N, Zhang BP, *et al.* Enhanced piezoelectric properties of $0.7BiFeO_3$-$0.3BaTiO_3$ lead-free piezoceramics with high Curie temperature by optimizing Bi self-compensation. *Ceram Int* 2019, **45**: 24382–24391.

[35] Feng JQ, Zhang YT, Song XL, *et al.* Strain evolution from the ferroelectric to the relaxor state in $(0.67 - x)BiFeO_3$–$0.33BaTiO_3$–$xBi(Mg_{0.5}Zr_{0.5})O_3$ lead-free ceramics. *Phys Chem Chem Phys* 2024, **26**: 24667–24675.

[36] Li CY, Zheng T, Wu JG. Competitive mechanism of temperature-dependent electrical properties in $BiFeO_3$-$BaTiO_3$ ferroelectrics controlled by domain evolution. *Acta Mater* 2021, **206**: 116601.

[37] Hao YJ, Gao XQ, Tang YC, *et al.* Enhanced strain of $BiFeO_3$-$BaTiO_3$ relaxor ferroelectrics ceramics: domain structure evolution induced by electric-fields and temperature. *Rare Met* 2025, **44**: 2661–2671.

[38] Ke SM, Huang HT, Fan HQ, *et al.* Antiferroelectric-like properties and enhanced polarization of Cu-doped $K_{0.5}Na_{0.5}NbO_3$ piezoelectric ceramics. *Appl Phys Lett* 2012, **101**: 082901.

[39] Lin JM, Qian J, Shi YJ, *et al.* Enhanced Piezoelectric Response Attained by Defect Dipoles in $BiFeO_3$-based Lead-Free Ceramics. *ACS Appl Mater Interfaces* 2024, **16**: 67959–67969.

[40] Xiao WR, Wu Y, Liu YL, *et al.* Enhanced electrocaloric effect in ferroelectric ceramics via defect dipole engineering. *Nat Commun* 2025, **16**: 8909.

[41] Eichel RA. Structural and dynamic properties of oxygen vacancies in perovskite oxides—analysis of defect chemistry by modern multi-frequency and pulsed EPR techniques. *Phys Chem Chem Phys* 2011, **13**: 368–84.

[42] Zhuk NA, Lutoev VP, Makeev BA, *et al.* EPR, NEXAFS study and magnetic properties of Fe-doped ferroelectric ceramics. *Rev Adv Mater Sci* 2018, **57**: 35–41.

[43] Meštrić H, Eichel RA, Kloss T, *et al.* Iron-oxygen vacancy defect centers in $PbTiO_3$: Newman superposition model analysis and density functional calculations. *Phys Rev B* 2005, **71**: 134109.

[44] Bykov I, Zagorodniy Y, Yurchenko L, *et al.* Using the methods of radiospectroscopy (EPR, NMR) to study the nature of the defect structure of solid solutions based on lead zirconate titanate (PZT). *IEEE Trans Ultrason Ferroelectr Freq Control* 2014, **61**: 1379–1385.

[45] Singh V, Chakradhar RPS, Rao JL, *et al.* EPR and photoluminescence properties of green light emitting $LaAl_{11}O_{18}:Mn^{2+}$ phosphors. *Phys B* 2012, **407**: 2289–2294.

[46] Zhuk NA, Lutoev VP, Belyy VA, *et al.* EPR and NEXAFS spectroscopy of $BiNb_{1-x}Fe_xO_{4-\delta}$ ceramics. *Phys B* 2019, **552**: 142–146.

[47] Paulin JV, Graeff CFO, Mostert AB. Decoding eumelanin's spin label signature: a comprehensive EPR analysis. *Mater Adv* 2024, **5**: 1395–1419.

Just Accepted

[48] Vugmeister BE. EPR study of internal field distribution, local order and dynamics in klt and KTN. *Ferroelectrics* 1993, **150**: 77–88.

[49] Weil JA, Bolton JR. *Electron Paramagnetic Resonance*. New Jersey (USA): John Wiley & Sons, Inc., 2007.

[50] Li B, Zheng T, Wu JG. Decoding thermal depolarization temperature in bismuth ferrite–barium titanate relaxor ferroelectrics with large strain response. *ACS Appl Mater Interfaces* 2021, **13**: 37422–37432.

[51] Zhang MH, Zhao CH, Yan XD, *et al.* Understanding the grain size dependence of functionalities in lead-free (Ba,Ca)(Zr,Ti)O_3. *Acta Mater* 2024, **276**: 120112.

[52] Bobrowski P, Faryna M, Pędzich Z. Microstructural characterization of yttria-stabilized zirconia sintered at different temperatures using 3D EBSD, 2D EBSD and stereological calculations. *J Mater Eng Perform* 2017, **26**: 4681–4688.

[53] Pabst W, Gregorová E, Uhlířová T. Microstructure characterization via stereological relations — a shortcut for beginners. *Mater Charact* 2015, **105**: 1–12.

[54] Nunes LM, Antonelli E, Bernardi MIB, *et al.* How grain boundaries modify the high-temperature dielectric response of ferroelectric electroceramics like $BaTiO_3$? *Mater Res Bull* 2011, **46**: 136–139.

[55] Ravikiran U, Zacharias E, Rajashekhar G, *et al.* Impedance spectroscopy studies on samarium and sodium substituted strontium bismuth titanate (SBTi). *Ceram Int* 2019, **45**: 15188-15198.

[56] Padurariu L, Curecheriu L, Buscaglia V, *et al.* Field-dependent permittivity in nanostructured $BaTiO_3$ ceramics: Modeling and experimental verification. *Phys Rev B* 2012, **85**: 224111.

[57] Mohanty S, Choudhary RNP. Dielectric and impedance characteristics of $KTaO_3$ modified $BiFeO_3$ multiferroics. *J Mater Sci: Mater Electron* 2014, **25**: 1180–1187.

[58] Badapanda T, Senthil V, Rout SK, *et al.* Rietveld refinement, microstructure, conductivity and impedance properties of $Ba[Zr_{0.25}Ti_{0.75}]O_3$ ceramic. *Curr Appl Phys* 2011, **11**: 1282–1293.

[59] Khondabi M, Ahmadvand H. Dynamics of polar nanoregions and relaxation mechanisms in $BiFeO_3$−$BaTiO_3$−$KNbO_3$ relaxor ferroelectric ceramics: a dielectric and impedance spectroscopy study. *Phys Chem C* 2024, **128**: 15732–15743.

[60] Tang XG, Liu QX, Wang J, *et al.* Electric-field dependence of dielectric properties of sol-gel derived $Ba(Zr_{0.2}Ti_{0.8})O_3$ ceramics. *Appl Phys A* 2009, **96**: 945–952.

[61] Fan GF, Zeng FF, Guo HT, *et al.* High-performance BF-BT-based lead-free piezoceramics with local polar nanoregions of room-temperature ergodic state. *J Alloys Compd* 2022, **925**: 166781.

[62] Yao ZK, Guo HT, Zeng H, *et al.* Defect engineering enables low-temperature synthesis of BF-BT piezoceramics with enhanced electric field-induced strain. *Appl Surf Sci* 2026, **729**: 166177.

Just Accepted

[63] Lin JF, Qian J, Ge GL, *et al.* Multiscale reconfiguration induced highly saturated poling in lead-free piezoceramics for giant energy conversion. *Nat Commun* 2024, **15**: 2560.

[64] Yin J, Liu G, Lv X, *et al.* Superior and anti-fatigue electro-strain in $Bi_{0.5}Na_{0.5}TiO_3$-based polycrystalline relaxor ferroelectrics. *J Mater Chem A* 2019, **7**: 5391–5401.

[65] Fu GH, Wang J, Zhang HM, *et al.* Deciphering the effect of defect dipoles on the polarization and electrostrain behavior in perovskite ferroelectrics. *Nano Lett* 2024, **24**: 12148–12155.

[66] Luo F, Jiang DH, Zhu YH, *et al.* Achieving large strain and low hysteresis in $BiFeO_3$-$BaTiO_3$-based piezoelectric ceramics. *Ceram Int* 2024, **50**: 27846–27855.

[67] Li B, Li CY, Zheng T, *et al.* Property regulation principle in Mn-doped BF–BT ceramics: competitive control of domain switching by defect dipoles and domain configuration. *Adv Electron Mater* 2022, **8**: 2200609.

[68] Lin JM, Liu B, Liu MX, *et al.* Manipulating piezoelectric and electro-strain properties of $BiFeO_3$-$BaTiO_3$-based ceramics through chemical doping-controlled domain-size engineering. *Acta Mater* 2025, **297**: 121379.

[69] Lu XY, Chen ZH, Cao Y, *et al.* Mechanical-force-induced non-local collective ferroelastic switching in epitaxial lead-titanate thin films. *Nat Commun* 2019, **10**: 3951.

[70] Li F, Zhang SJ, Yang TN, *et al.* The origin of ultrahigh piezoelectricity in relaxor-ferroelectric solid solution crystals. *Nat Commun* 2016, **7**: 13807.

[71] Smith RC, Ounaies Z. A domain wall model for hysteresis in piezoelectric materials. *J Intell Mater Syst Struct* 2000, **11**: 62–79.

[72] Lin JM, Guo XW, Liu B, *et al.* Exceptionally large thickness-independent longitudinal strain in lead-free piezoceramics via defect dipole engineering. *Adv Funct Mater* 2025, **36**: e22553.

[73] Nie XR, Jing RY, Chen FK, *et al.* Synergistic phase boundary and defect engineering enables ultrahigh electrostrain in lead-free ceramics. *Adv Funct Mater* 2025, **36**: e13360.

[74] Liu J, Zhang GL, Liu S, *et al.* Hysteresis-free electrostrictive response in PMN-PT ceramics and multilayer actuators. *Ceram Int* 2026, **52**: 33906–33914.

[75] Ma ZX, Nie WY, Sun MZ, *et al.* Li^+ and Nb^{5+} codoped BNT-based ceramic with ultrahigh electrostrain under a moderate electric field. *J Adv Ceram* 2026, **15**: 9221309.

[76] Nie XR, Jing RY, Zhang LY, *et al.* Coupled phase-boundary engineering and defect control for ultrahigh electrostrain with low hysteresis in lead-free BNBT-based ceramics. *Acta Mater* 2026, **313**: 122284.

[77] Zeng H, Luan YH, Yao ZK, *et al.* High electrostrain and low hysteresis enabled by domain engineering and defect strategy in BF-BT-based lead-free piezoceramics. *Mater Today Phys* 2026, **67**: 102188.

Just Accepted

Just Accepted